2024 IEEE/RSJ International Conference on Intelligent Robots and Systems (IROS)
October 14-18, 2024. Abu Dhabi, UAE

Development of a Novel Redundant Parallel Mechanism with Enlarged Workspace and Enhanced Dexterity for Fracture Reduction Surgery

Quan Yuan, Xu Liang, Tingting Su, and Weibang Bai

***Abstract*— The limited workspace and complex singularity issues are predominant factors impeding the clinical applicability of fracture reduction parallel robots. To address these challenges, this paper proposes a novel redundant parallel mechanism (NRPM) for robotic-assisted fracture reduction with an enlarged workspace and enhanced dexterity capabilities based on the traditional Stewart parallel mechanism (SPM). With six redundant degrees-of-freedom (DOFs) added to the novel mechanism, the kinematics of NRPM needs to be thoroughly analyzed. Furthermore, the calculation of its workspace and determination of its dexterity are deduced. Both the analytical simulation and real experiment results demonstrated the effectiveness and superior performance of the proposed NRPM compared to SPM.**

I. INTRODUCTION

Fracture reduction is a common and crucial orthopedic surgery that aims to align and fix broken bones, requiring high operation precision, large reduction force, as well as large workspace [1], [2]. However, in traditional surgery, doctors are exposed to radiation for extended periods, and maintaining consistent manual precision is challenging [3], [4]. Whereas, surgical robots [5], [6] are advantageous in radiation avoidance, high-precision, and flexible operation. It is therefore necessary to develop a surgical robot to assist or even release the doctor in the reduction surgery.

Due to the crucial requirements of precision and force in fracture reduction surgery, it is obvious that parallel robots are more suitable for orthopedic surgery than serial robots due to their advantages of high precision, large load capacity, and compact structure [7], [8]. Many scholars have developed parallel robots for fracture reduction surgery. Tang et al. [9] proposed a hexapod mechanism for surgery based on the Stewart platform. Mukherjee et al. [10] introduced an adaptable parallel robotic system designed for fracture reduction. Kara et al. [11] developed a computer-assisted external fixator system based on the Stewart parallel platform.

Although parallel robots offer advantages in performance, they still exhibit certain disadvantages, including limited workspace and complex singularities [12]. However, the robotic-assisted fracture reduction surgery still requires adequate workspace [2]. Introducing redundant components to a parallel mechanism is a viable solution for expanding its workspace and mitigating singularity issues [13]. Chen et al. [14] proposed a novel redundant (6+1) DOFs parallel mechanism with the configurable platform. The workspace analysis, singularity analysis, and numerical verification were conducted. Zhao et al. [15] proposed a novel symmetric parallel 6-RPS mechanism with multi-redundant actuation, and its accessible workspace can be within the high-performance workspace. Liang et al. [16] designed a redundant parallel mechanism (RPM) and the analysis results showed that RPM has better performances in workspace and singularity compared to the Stewart parallel mechanism (SPM). Those proposed redundant parallel mechanisms achieved better performances to some extent, however, it still needs further improvement, especially in terms of large workspace and singularity-free. Inspired by this concept, we propose and develop a novel redundant parallel mechanism (NRPM) in this paper, with a comprehensive comparison with SPM subsequently.

II. KINEMATIC MODELING

A. General Design

Firstly, the CAD model of designed NRPM and SPM are illustrated in Fig. 1. The fixing coordinate frame $\mathrm{O(X, Y, Z)}$ is established at the intersection of the projections of the three tilted slides on the fixing frame, where the X-axis is collinear with a projection of the tilted slide, and the Z-axis is perpendicular to the fixing frame. The coordinate frame of the moving frame $\mathrm{O'(X', Y', Z')}$ is located at its center point. The NRPM is composed of a moving frame, six links, three tilted sliders, three tilted slides, a central base, and a fixing frame. The link is used to support and drive the moving frame. Combining the tilted slide, central base, and links will enhance the moving frame's workspace and dexterity. The bottom of the tilted slide is connected with the revolute joint on the base slide, and the top is connected with the central base. The angle range between the tilted slide and fixing frame is set as $[0°, 45°]$. The three revolute joints are evenly fixed on the fixing frame around the circumference, i.e. with the same angle of $120°$. In Fig. 1(b), the sizes of the moving frame and fixing frame are the same as those of NRPM. The stroke of the long link is the same as the stroke of the link of NRPM. During the fracture reduction surgery, the NRPM can be firstly fixed to a base, such as the surgical bed, with three Kirschner wires securing the broken bone. The objective limb can be immobilized, and then the

This work is supported by the Shanghai Pujiang Program (2023X0203-101-02), Shanghai Frontiers Science Center of Human-centered Artificial Intelligence (ShangHAI), MoE Key Laboratory of Intelligent Perception and Human-Machine Collaboration (KLIP-HuMaCo), and the Natural Science Foundation of China (62373013). *(Corresponding author: Weibang Bai)*

Quan Yuan and Weibang Bai are with the ShanghaiTech Automation and Robotics (STAR) Center, School of Information Science and Technology, ShanghaiTech University, Shanghai, 201210, China.

Xu Liang is with the School of Automation and Intelligence, Beijing Jiaotong University, Beijing, 100044, China.

Tingting Su is with the Faculty of Information Technology, Beijing University of Technology, Beijing, 100124, China.

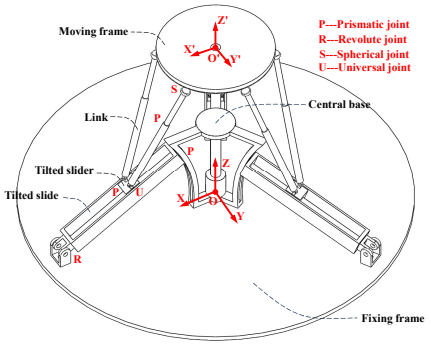

(a)

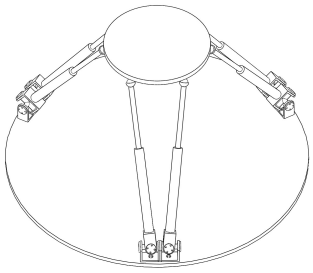

(b)

Fig. 1: (a) CAD model of NRPM, (b) CAD model of SPM.

NRPM's moving platform can be operated to complete the reduction processes.

B. Kinematics of NRPM

The NRPM diagram and the top view of the moving frame are illustrated in Fig. 2(a) and Fig. 2(b) respectively. It should be noted that all the revolute joints, and all the prismatic joints except those on the central base are active. In Fig. 3(a), the corresponding active prismatic joints are moving along $A_i^j C_i^j (i = 1, 2, 3; j = 1, 2)$ and $B_i^j D_i^j (i = 1, 2, 3; j = 1, 2)$, and the active revolute joints are rotating around the axis through $A_i (i = 1, 2, 3)$. As shown in Fig. 2(b), the radius of the moving frame is a. B_1^1 and B_1^2 are symmetric about the X′-axis, and their distance is $2b$.

To derive the inverse kinematics solution of the moving frame, the Euler angles of its orientation in z-y-x order can be expressed as (ψ, θ, φ). The transformation matrix from the moving frame to the fixing frame can be expressed as

$$\mathbf{R}_1 = \mathbf{R}_z(\psi)\mathbf{R}_y(\theta)\mathbf{R}_x(\varphi) = \begin{bmatrix} c\psi c\theta & -s\psi c\varphi + c\psi s\theta s\varphi & s\psi s\varphi + c\psi s\theta c\varphi \\ s\psi c\theta & c\psi c\varphi + s\psi s\theta s\varphi & -c\psi s\varphi + s\psi s\theta c\varphi \\ -s\theta & c\theta s\varphi & c\theta c\varphi \end{bmatrix} \tag{1}$$

where c and s represent cosine and sine respectively.

The position vector of $\boldsymbol{B}_i^j (i = 1, 2, 3; j = 1, 2)$ in the fixing frame can be expressed as

$$\boldsymbol{B}_i^j = \boldsymbol{P}_o + \boldsymbol{R}_1 \bar{\boldsymbol{u}}_i^j \tag{2}$$

where $\boldsymbol{P}_o$ is the position vector of O' in the fixing frame. $\bar{\boldsymbol{u}}_i^j$ denotes the position vector of point B_i^j in the moving frame, and it can be expressed as

$$\bar{\boldsymbol{u}}_i^j = \boldsymbol{Z}_i \begin{bmatrix} \sqrt{a^2 - b^2} & (-1)^{j+1} b & 0 \end{bmatrix}^{\mathrm{T}} \tag{3}$$

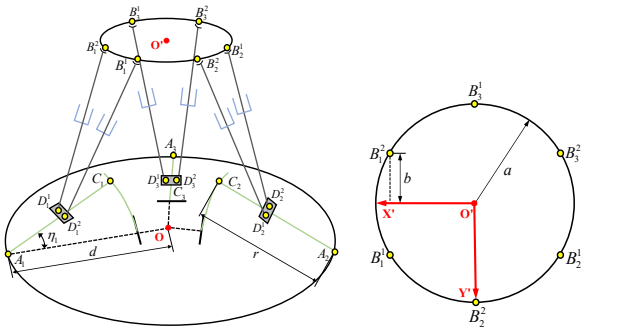

(a) (b)

Fig. 2: (a) Diagram of NRPM, (b) Top view of the moving frame.

where

$$\boldsymbol{Z}_i = \begin{bmatrix} c\gamma_i & -s\gamma_i & 0 \\ s\gamma_i & c\gamma_i & 0 \\ 0 & 0 & 1 \end{bmatrix} \tag{4}$$

where $\gamma_1 = 0$, $\gamma_2 = 2\pi/3$, and $\gamma_3 = 4\pi/3$ are the angles of each projection of tilted slide in the fixing frame.

The vector $\boldsymbol{u}_i^j$ in the fixing frame can be expressed as

$$\boldsymbol{u}_i^j = \boldsymbol{R_1} \bar{\boldsymbol{u}}_i^j \tag{5}$$

The relationship between the angular velocity and the derivative of the orientation of the moving platform in the fixing frame can be expressed as

$$\boldsymbol{\omega} = \boldsymbol{R}_2 \dot{\boldsymbol{\Theta}} \tag{6}$$

where $\boldsymbol{\Theta} = \begin{bmatrix} \varphi & \theta & \psi \end{bmatrix}^T$ denotes the orientation of the moving frame, and $\boldsymbol{R}_2$ can be expressed as

$$\boldsymbol{R}_2 = \begin{bmatrix} c\theta c\varphi & -s\varphi & 0 \\ c\theta s\varphi & c\varphi & 0 \\ -s\theta & 0 & 1 \end{bmatrix} \tag{7}$$

The velocity vector of B_i^j can be obtained by the time derivative of Eq. (2)

$$\dot{\boldsymbol{B}}_i^j = \dot{\boldsymbol{P}}_o + \boldsymbol{\omega} \times \boldsymbol{u}_i^j \tag{8}$$

Eq. (8) can be rewritten as

$$\dot{\boldsymbol{B}}_i^j = \begin{bmatrix} \boldsymbol{I}_{3\times3} & -\tilde{\boldsymbol{u}}_i^j \boldsymbol{R_2} \end{bmatrix} \begin{bmatrix} \dot{\boldsymbol{P}}_o \\ \dot{\boldsymbol{\Theta}} \end{bmatrix} \tag{9}$$

where $\tilde{\boldsymbol{u}}_i^j$ is the skew symmetric matrix of $\boldsymbol{u}_i^j$.

The position vector of C_i in the fixing frame can be expressed as

$$\boldsymbol{C}_i = \boldsymbol{Z}_i \begin{bmatrix} d - rc\eta_i & 0 & rs\eta_i \end{bmatrix}^T \tag{10}$$

where η_i denotes the angle between the i-th tilted slide and the fixing frame. The time derivative of Eq. (10) can be derived as

$$\dot{\boldsymbol{C}}_i = \boldsymbol{h}_i \dot{\eta}_i \tag{11}$$

where

$$\boldsymbol{h}_i = \begin{bmatrix} rc\gamma_i s\eta_i & rs\gamma_i s\eta_i & rc\eta_i \end{bmatrix}^T \tag{12}$$

Then, the position vector of D_i^j in the fixing frame can

be expressed as

$$\boldsymbol{D}_i^j = \boldsymbol{C}_i^j - m_i \boldsymbol{s}_i + d' \boldsymbol{j}_i^j = \boldsymbol{B}_i^j - l_i^j \boldsymbol{t}_i^j \tag{13}$$

where m_i denotes the distance that the i-th slider moves in the tilted slide, $\boldsymbol{s}_i$ denotes the unit vector of the i-th tilted slide, d' denotes the distance from D_1^2 to the midpoint of $D_1^1 D_1^2$, $\boldsymbol{j}_i^j = \begin{bmatrix} 0 & (-1)^j d' & 0 \end{bmatrix}^T$, l_i^j denotes the length of the ij-th link, and $\boldsymbol{t}_i^j$ denotes the unit vector of the ij-th link.

Then, the length of l_i^j is obtained as

$$l_i^j = \left\| \boldsymbol{B}_i^j - \boldsymbol{D}_i^j \right\| \tag{14}$$

The position and orientation of the moving frame are denoted by $\boldsymbol{x} = \begin{bmatrix} \boldsymbol{P}_o & \boldsymbol{\Theta} \end{bmatrix}^{\mathrm{T}}$. The lengths of the actuators are denoted by $\boldsymbol{q} = \begin{bmatrix} \boldsymbol{q}_1 & \boldsymbol{q}_2 & \boldsymbol{q}_3 \end{bmatrix}^{\mathrm{T}}$, where

$$\boldsymbol{q}_1 = \begin{bmatrix} l_1^1 & l_1^2 & l_2^1 & l_2^2 & l_3^1 & l_3^2 \end{bmatrix} \tag{15}$$

$$\boldsymbol{q}_2 = \begin{bmatrix} m_1 & m_2 & m_3 \end{bmatrix} \tag{16}$$

$$\boldsymbol{q}_3 = \begin{bmatrix} \eta_1 & \eta_2 & \eta_3 \end{bmatrix} \tag{17}$$

The velocity vector of $\boldsymbol{D}_i^j$ can be obtained by the derivatives of Eq. (13).

$$\begin{aligned} \dot{\boldsymbol{D}}_i^j &= \dot{\boldsymbol{C}}_i - (\dot{m}_i \boldsymbol{s}_i + m_i \boldsymbol{\Omega}_i \times \boldsymbol{s}_i) + (\dot{d}' \boldsymbol{j}_i^j + d' \boldsymbol{J}_i^j \times \boldsymbol{j}_i^j) \\ &= \dot{\boldsymbol{B}}_i^j - (\dot{l}_i^j \boldsymbol{t}_i^j + l_i^j \boldsymbol{\Pi}_i^j \times \boldsymbol{t}_i^j) \end{aligned} \tag{18}$$

where $\boldsymbol{\Omega}_i$, $\boldsymbol{J}_i^j$, and $\boldsymbol{\Pi}_i^j$ denote the angular velocities of the i-th tilted slide, $\boldsymbol{j}_i^j$, and the ij-th link respectively.

We can get $\boldsymbol{s}_i \cdot \boldsymbol{\Omega}_i = \dot{d}' \cdot \boldsymbol{j}_i^j = \boldsymbol{j}_i^j \cdot \boldsymbol{J}_i^j = \boldsymbol{t}_i^j \cdot \boldsymbol{\Pi}_i^j = 0$. Then, multiply $\boldsymbol{t}_i^j$ on both sides of Eq. (18), then $\dot{l}_i^j$ can be obtained

$$\dot{l}_i^j = \boldsymbol{t}_i^j (\dot{\boldsymbol{B}}_i^j - \dot{\boldsymbol{C}}_i + \dot{m}_i \boldsymbol{s}_i) \tag{19}$$

According to Eq. (9), Eq. (11) and Eq. (19), $\dot{l}_i^j$ can be rewritten as

$$\dot{l}_i^j = \boldsymbol{t}_i^{j\mathrm{T}} \begin{bmatrix} \boldsymbol{I}_{3\times 3} & -\tilde{\boldsymbol{u}}_i^j \boldsymbol{R}_2 \end{bmatrix} \begin{bmatrix} \dot{\boldsymbol{P}}_o \\ \dot{\boldsymbol{\Theta}} \end{bmatrix} - \boldsymbol{t}_i^{j\mathrm{T}} \boldsymbol{h}_i \dot{\eta}_i + \boldsymbol{t}_i^{j\mathrm{T}} \boldsymbol{s}_i \dot{m}_i \tag{20}$$

Eq. (20) can be represented as

$$\boldsymbol{J}_x \dot{\boldsymbol{x}} = \boldsymbol{J}_q \dot{\boldsymbol{q}} \tag{21}$$

where $\boldsymbol{J}_x$ is the direct Jocabian matrix of 6×6 and $\boldsymbol{J}_q$ is the inverse Jacobian matrix of 6×12, and can be represented as

$$\boldsymbol{J}_x = \begin{bmatrix} \boldsymbol{J}_1^1 \\ \boldsymbol{J}_1^2 \\ \boldsymbol{J}_2^1 \\ \boldsymbol{J}_2^2 \\ \boldsymbol{J}_3^1 \\ \boldsymbol{J}_3^2 \end{bmatrix}_{6\times 6} \tag{22}$$

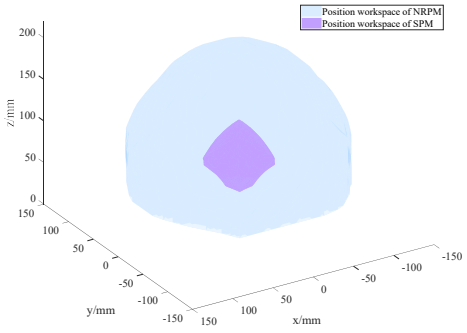

Fig. 3: Position workspaces of NRPM and SPM.

$$\boldsymbol{J}_q = \begin{bmatrix} 1 & 0 & 0 & 0 & 0 & 0 & e_1^1 & 0 & 0 & f_1^1 & 0 & 0 \\ 0 & 1 & 0 & 0 & 0 & 0 & e_1^2 & 0 & 0 & f_1^2 & 0 & 0 \\ 0 & 0 & 1 & 0 & 0 & 0 & 0 & e_2^1 & 0 & 0 & f_2^1 & 0 \\ 0 & 0 & 0 & 1 & 0 & 0 & 0 & e_2^2 & 0 & 0 & f_2^2 & 0 \\ 0 & 0 & 0 & 0 & 1 & 0 & 0 & 0 & e_3^1 & 0 & 0 & f_3^1 \\ 0 & 0 & 0 & 0 & 0 & 1 & 0 & 0 & e_3^2 & 0 & 0 & f_3^2 \end{bmatrix} \tag{23}$$

where

$$\boldsymbol{J}_i^j = \boldsymbol{t}_i^{j\mathrm{T}} \begin{bmatrix} \boldsymbol{I}_{3\times 3} & -\tilde{\boldsymbol{u}}_i^j \boldsymbol{R}_2 \end{bmatrix} \tag{24}$$

$$\begin{cases} e_i^j = \boldsymbol{t}_i^{j^T} \boldsymbol{h}_i \\ f_i^j = -\boldsymbol{t}_i^{j^T} \boldsymbol{s}_i \end{cases} \tag{25}$$

To obtain a dimensionally homogeneous Jacobian matrix $\boldsymbol{J}_{dh}$ [17], the last three columns of the direct Jacobian matrix are divided by $L = a/2$, which is the characteristic length of NRPM. The overall Jacobian matrix can be written as

$$\boldsymbol{J} = \boldsymbol{J}_{dh}^{-1} \boldsymbol{J}_q \tag{26}$$

III. Workspace Analysis

In this paper, the position workspace is defined as a collection of all space points that can be reached by the moving frame. Based on the kinematics of NRPM, the workspace of NRPM can be calculated. The geometric parameters of NRPM are listed in Table I. The workspace volume in parallel mechanisms is primarily influenced by the link length limitation, link interference, and joint angle restriction. The calculation of the workspace for NRPM doesn't consider the joint angle restriction as a primary factor, thus ignoring its influence on the workspace volume. Determining whether the two links interfere with each other mainly depends on the minimum distance between them. The minimum distance can be obtained through a multi-step algorithm [18]. The redundant mechanisms usually have infinite inverse solutions, so m_i, η_i are traversed to get a unique solution for each link. The position workspaces of SPM and NRPM are calculated and shown in Fig. 3.

The orientation workspace refers to a collection of all orientations that can be attained by the moving frame at a prescribed position. In this paper, the center point O′ of the moving frame is fixed at a specific point (0, 0, 160). The orientation workspace of NRPM is calculated by traversing each feasible orientation of its moving frame over a relatively large workspace, which covers its orientation workspace.

TABLE I: Geometric parameters of NRPM

a (mm)	60
b (mm)	30
d (mm)	160
d' (mm)	20
$m_{i\,\max}$ (mm)	120
r (mm)	140
l_i^j (mm)	$[90, 175]$
η_i (deg)	$[0, 45]$

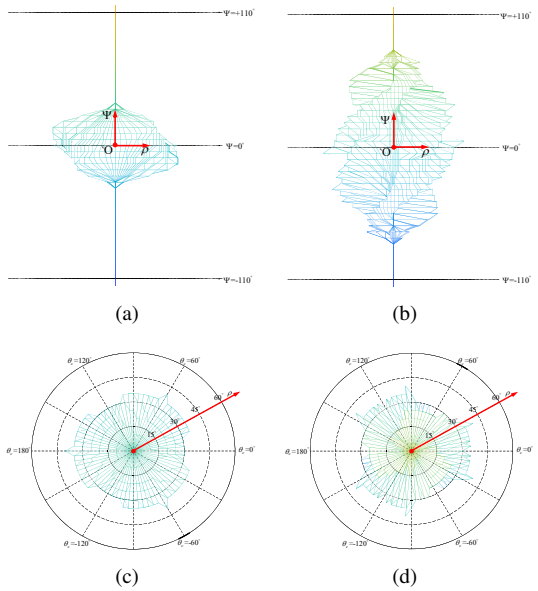

Fig. 4: (a) Cross-section of orientation workspace of SPM in ρ-O-Ψ direction. (b) Cross-section of orientation workspace of NRPM in ρ-O-Ψ direction. (c) Top view of the orientation workspace of SPM. (d) Top view of the orientation workspace of NRPM.

The tilt angle and torsion angle are used to represent the orientation of the moving frame [19]. With the method in the literature [20], the orientation workspace of NRPM is represented in cylindrical coordinate (Ψ, ρ, θ_c), where Ψ denotes the torsion angle, ρ denotes the magnitude of tilt angle, and θ_c denotes the tilt direction of the center axis of the moving platform. The orientation workspaces of NRPM and SPM are illustrated in Fig. 4.

The comparison results are shown in Table II. It can be seen that the volume of NRPM is about 41 times larger than that of the SPM. NRPM has a more extensive position workspace in the horizontal and vertical directions. In addition, the results also indicate that NRPM has a larger orientation workspace and a more extensive torsion angle range. Besides, their tilt angle ranges are similar.

IV. Singularity Analysis

Mechanisms in singularities may be out of control and lose their stiffness or dexterity [21]. Generally, singularities encountered in close-loop kinematic chains are classified into three categories [22], i.e., $|\boldsymbol{J}_x| = 0$, $|\boldsymbol{J}_q| = 0$, and $|\boldsymbol{J}_x| = |\boldsymbol{J}_q| = 0$. However, it is difficult to determine

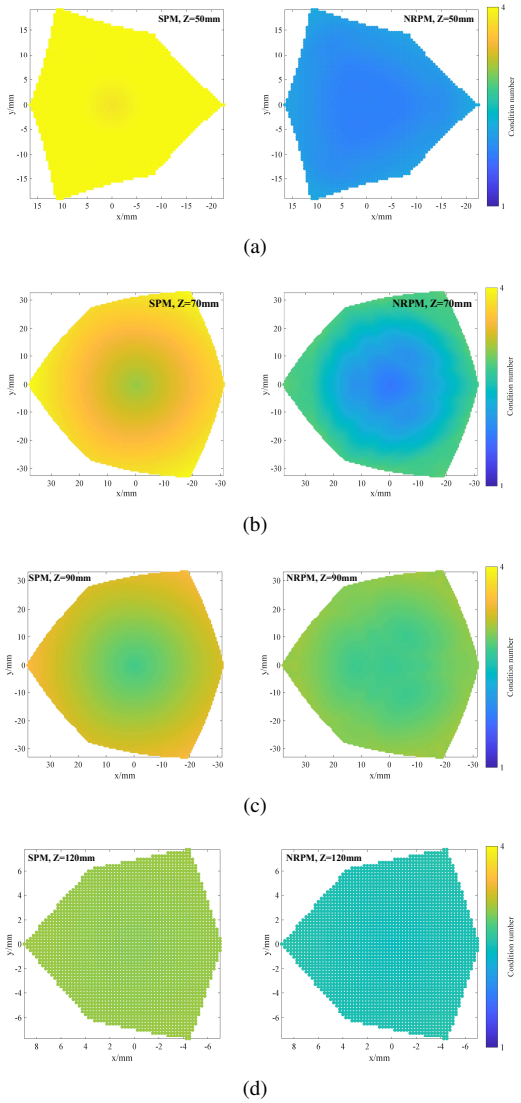

Fig. 5: Cross-sections in X-O-Y direction of the condition number distributions of NRPM and SPM in the position workspace of SPM when z=50, 70, 90, 120mm. (a) z=50mm. (b) z=70mm. (c) z=90mm. (d) z=120mm. All four compared situations indicate that the condition number distribution of NRPM is much lower than SPM.

whether the determinant value of NRPM's Jacobian matrix is 0. Therefore, the condition number is introduced to judge the singularity and evaluate the dexterity of NRPM [23]. The condition number can be calculated as

$$\text{condition number} = \|\boldsymbol{J}\| \left\|\boldsymbol{J}^{-1}\right\| \tag{27}$$

Its range falls within the interval $[1, \infty)$. When the obtained condition number $= 1$, it can be assumed that the motion performance of the mechanism is the best, while when condition number $\to \infty$, it can be assumed that the motion performance of the mechanism is the worst.

The condition number distribution of NRPM in the position workspace is compared with that of SPM to analyze their motion performance. Cross-sections in X-O-Y direction of the condition number distribution of NRPM and SPM are

TABLE II: Workspace Analysis Results

	Volume (mm^3)	Hor. displacement (mm)	Ver. displacement (mm)	Torsion angle (deg)	Tilt angle (deg)
SPM	1.7211×10^5	104	110	35	40
NRPM	6.9913×10^6	196	296	79	41

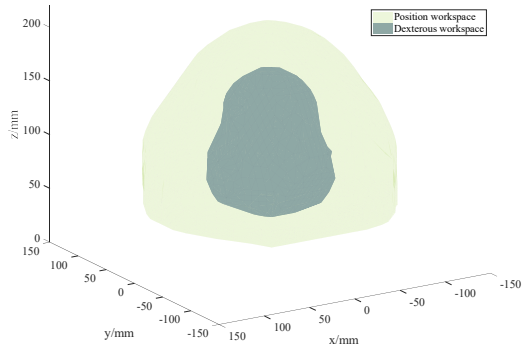

Fig. 6: Position and dexterous workspaces of NRPM.

illustrated in Fig. 5. In each cross-section, all four compared situations indicate that the condition number distribution of NRPM is much lower than SPM. Besides, the overall condition number range of NRPM is $[1.6841, 3.1061]$, and the condition number range of SPM is $[2.7392, 9.9373]$. The condition number data of NRPM are more concentrated around a much lower value than that of SPM. Thus, it can be concluded that NRPM has better performance in singularity than SPM in the position workspace.

Generally, parallel mechanisms are recommended to be operated in the dexterous workspace, as the mechanisms can achieve more stable motion performance [24]. In this paper, the dexterous workspace is defined and illustrated as the space with the condition numbers of the points' $\boldsymbol{J}$ lower than a maximum threshold. Because the volume of the dexterous workspace will drop rapidly when the condition number of $\boldsymbol{J}$ is smaller than 3.30, the maximum threshold limitation is chosen as 3.30. The position and dexterous workspaces of NRPM are illustrated in Fig. 6. It can be calculated that the dexterous workspace is approximately 16.05% of the position workspace. In the application scenario, NRPM should be operated in the dexterous workspace as much as possible.

V. Experiments

In this section, the prototype of NRPM is fabricated using 3D printing technology. The resin material is selected to print the prototype. For consistency with the analysis in Section III, the geometric parameters of the prototype are selected from Table I.

The workspace experiments encompass two components: a position workspace test and an orientation workspace test. The position workspace experiment aims to validate the analytical results outlined in Section III by determining the maximum horizontal and vertical displacements of the moving frame. In this experiment, the orientation of the moving frame remains constant. The displacement of point O′ was measured manually. Fig. 7(a) illustrates the initial position and orientation of the prototype. Fig. 7(b)-(d) present the minimum vertical displacement, maximum vertical displacement, and maximum horizontal displacement of the moving frame respectively. Extra Wedges in Fig. 7(c) and Fig. 7(d) are set to support the tilted slides in fixed positions and orientations for the convenience of measurement.

The orientation workspace experiment aims to acquire the tilt and torsion angles of the moving frame to corroborate the

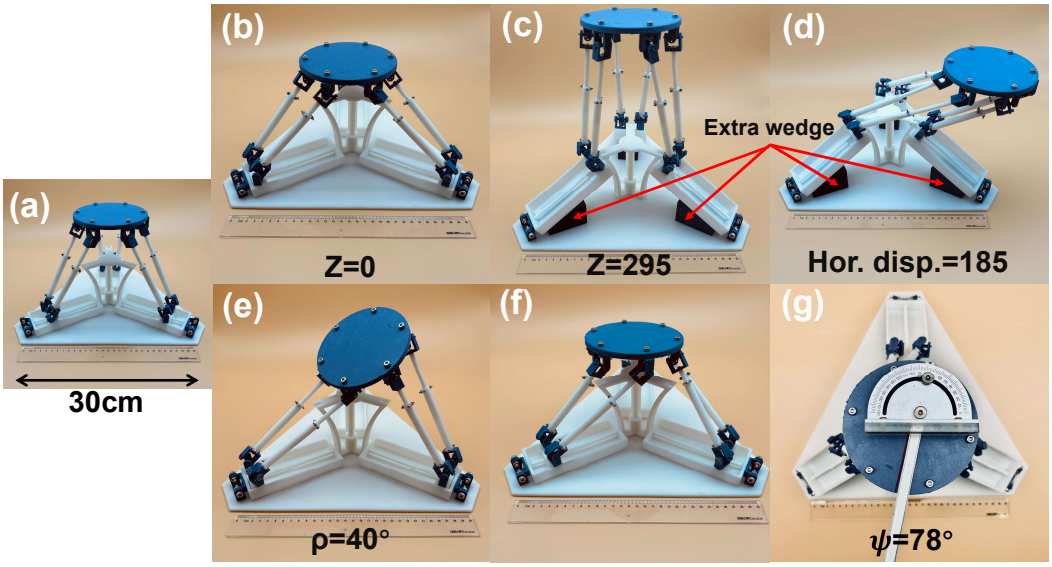

Fig. 7: Different position and orientation tests of NRPM. (a) Initial position and orientation. (b) Minimum vertical displacement. (c) Maximum vertical displacement. (d) Maximum horizontal displacement. (e) Maximum tilt angle. (f) Maximum torsion angle. (g) Top view of maximum torsion angle. The extra supporting wedges in the figure are manually added for the convenience of measurement.

TABLE III: Comparison of simulation and experimental workspace results.

Maximum items	Sim.	Exp.	Error
Hor. displacement (mm)	296	295	0.03%
Ver. displacement (mm)	196	185	5.61%
Torsion angle (deg)	79	78	1.27%
Tilt angle (deg)	41	40	2.44%

analytical results in Section III. Throughout this experiment, the position of the moving frame remains constant. The maximum torsion angle and maximum tilt angle of the moving frame are depicted in Fig. 7(e)-(f) respectively. Fig. 7(g) illustrates top view of the prototype when the torsion angle is the maximum.

The simulation and experimental results are listed in Table III. The experimental results closely align with the simulation data with an acceptable margin of error. Thus, it can be concluded that the methodologies for workspace analysis in Section III are effective, and the proposed and developed NRPM can achieve a significantly enlarged workspace than SPM, which can be more suitable for the highly demanded fracture reduction surgery.

VI. Conclusion

In this paper, a novel redundant parallel mechanism (NRPM) for fracture reduction surgery is proposed and developed based on the traditional Stewart parallel mechanism (SPM). The kinematics of NRPM is deduced, and its workspaces are calculated. The analytical results show that the position workspace of NRPM is about 41 times larger than that of SPM, and the orientation workspace of NRPM is also larger, providing a broader range in terms of both tilt and torsion angles. The dexterity of NRPM is analyzed utilizing the condition number, and the dexterous workspace of NRPM is determined accordingly. The results indicate that NRPM outperforms SPM in terms of dexterity performance.

The proposed NRPM can offer a significantly enlarged workspace and achieve superior dexterity compared to SPM. Consequently, a prototype of the designed NRPM was developed, followed by experiments to validate its effectiveness. The experimental tests confirmed the analytical results, demonstrating its feasibility and applicability for robotic-assisted fracture reduction surgery, which demands high precision, significant force, and sufficient workspace for dexterous operation. In future work, we plan to conduct phantom surgical experiments to further evaluate and confirm the overall superior performance of our proposed NRPM for fracture reduction surgery.

References

[1] M. Oszwald, R. Westphal, J. Bredow, A. Calafi, T. Hufner, F. Wahl, C. Krettek, and T. Gosling, "Robot-assisted fracture reduction using three-dimensional intraoperative fracture visualization: An experimental study on human cadaver femora," *J. Orthop. Res.*, vol. 28, no. 9, pp. 1240–1244, 2010.

[2] J.-X. Zhao, C. Li, H. Ren, M. Hao, L.-C. Zhang, and P.-F. Tang, "Evolution and current applications of robot-assisted fracture reduction: a comprehensive review," *Annals of biomedical engineering*, vol. 48, pp. 203–224, 2020.

[3] R. Westphal, S. Winkelbach, F. Wahl, T. Gösling, M. Oszwald, T. Hüfner, and C. Krettek, "Robot-assisted long bone fracture reduction," *Int. J. Robot. Res.*, vol. 28, no. 10, pp. 1259–1278, 2009.

[4] T. Gosling, R. Westphal, T. Hufner, J. Faulstich, M. Kfuri, F. Wahl, and C. Krettek, "Robot-assisted fracture reduction: A preliminary study in the femur shaft," *Med. Biol. Eng. Comput.*, vol. 43, pp. 115–120, 2005.

[5] X. Zhi, W. Bai, and E. M. Yeatman, "Kinematic parameter optimization of a miniaturized surgical instrument based on dexterous workspace determination," in *2021 6th IEEE International Conference on Advanced Robotics and Mechatronics (ICARM)*. IEEE, 2021, pp. 112–118.

[6] F. Cursi, W. Bai, E. M. Yeatman, and P. Kormushev, "Task accuracy enhancement for a surgical macro-micro manipulator with probabilistic neural networks and uncertainty minimization," *Trans. Autom. Sci. Eng.*, 2022.

[7] M. Isaksson, "Kinematically redundant planar parallel mechanisms for optimal singularity avoidance," *J. Mech. Design*, vol. 139, no. 4, p. 042302, 2017.

[8] B. Chen, Q. Cao, and W. Bai, "A design of surgical robotic system based on 6-dof parallel mechanism," in *BIBE 2018; International Conference on Biological Information and Biomedical Engineering*. VDE, 2018, pp. 1–5.

[9] P. Tang, L. Hu, H. Du, M. Gong, and L. Zhang, "Novel 3d hexapod computer-assisted orthopaedic surgery system for closed diaphyseal fracture reduction," *Int. J. Med. Robot. Comp.*, vol. 8, no. 1, pp. 17–24, 2012.

[10] S. Mukherjee, M. Rendsburg, and W. Xu, "Surgeon-instructed, image-guided and robot-assisted long bone fractures reduction," in *1st international conference on sensing technology*. Citeseer, 2005, pp. 78–84.

[11] A. Kara, H. Celik, A. Seker, O. Karakoyun, R. Armagan, E. Kuyucu, and M. Erdil, "Treatment of open fractures with a computer-assisted external fixator system without the use of fluoroscopy," *Journal of orthopaedic surgery and research*, vol. 11, pp. 1–6, 2016.

[12] X. Liang, X. Zeng, G. Li, W. Chen, T. Su, and G. He, "Design, analysis, and optimization of a kinematically redundant parallel robot," in *Actuators*, vol. 12, no. 3. MDPI, 2023, p. 120.

[13] M. Luces, J. K. Mills, and B. Benhabib, "A review of redundant parallel kinematic mechanisms," *J. Intell. Robot. Syst.*, vol. 86, pp. 175–198, 2017.

[14] J. Yue, C. Lin, S. Jiang, W. Li, F. Gao, and W. Chen, "Design, analysis and optimization of a novel redundant (6+ 1)-degree-of-freedom parallel mechanism with configurable platform," *Mech. Mach. Theory*, vol. 192, p. 105550, 2024.

[15] R. Chen and J. Yao, "Kinematic performance analysis and dimensional optimization of new symmetric parallel mechanism 6rps with multi-redundant actuations," *J. Mech. Robot.*, vol. 16, pp. 081 002–1, 2024.

[16] T. Su, Q. Yuan, X. Liang, Y. Yan, H. Zhang, X. Jian, G. He, and Q. Zhao, "Design and analysis of a novel redundant parallel mechanism for long bone fracture reduction," *J. Mech. Robot.*, vol. 16, no. 8, 2024.

[17] O. Ma and J. Angeles, "Optimum architecture design of platform manipulators," in *Fifth International Conference on Advanced Robotics' Robots in Unstructured Environments*. IEEE, 1991, pp. 1130–1135.

[18] O. Masory and J. Wang, "Workspace evaluation of stewart platforms," *Adv. Robotics*, vol. 9, no. 4, pp. 443–461, 1994.

[19] I. Bonev, D. Zlatanov, and C. M. Gosselin, "Advantages of the modified euler angles in the design and control of pkms," in *2002 Parallel Kinematic Machines International Conference*. Citeseer, 2002, pp. 171–188.

[20] C. Gosselin and L.-T. Schreiber, "Kinematically redundant spatial parallel mechanisms for singularity avoidance and large orientational workspace," *IEEE Trans. Robot.*, vol. 32, no. 2, pp. 286–300, 2016.

[21] J. Song, C. Zhao, K. Zhao, W. Yan, and Z. Chen, "Singularity analysis and dimensional synthesis of a 2r1t 3-upu parallel mechanism based on performance atlas," *J. Mech. Robot.*, vol. 15, no. 1, p. 011001, 2023.

[22] C. Gosselin, J. Angeles *et al.*, "Singularity analysis of closed-loop kinematic chains." *IEEE Trans. Robot. Automat.*, vol. 6, no. 3, pp. 281–290, 1990.

[23] F. Zhao, S. Guo, C. Zhang, H. Qu, and D. Li, "Singularity analysis and dexterity performance on a novel parallel mechanism with kinematic redundancy," *Int. J. Adv. Robot. Syst.*, vol. 16, no. 5, p. 1729881419872641, 2019.

[24] G. Pond and J. A. Carretero, "Quantitative dexterous workspace comparison of parallel manipulators," *Mech Mach. Theory*, vol. 42, no. 10, pp. 1388–1400, 2007.